The Astrophysical Journal, 622:492–502, 2005 March 20

GAMMA-RAY SPECTRAL STATE TRANSITIONS OF GRO J1719−24

J. C. Ling
Jet Propulsion Laboratory, MS 169-327, California Institute of Technology, 4800 Oak Grove Drive, Pasadena, CA 91109; james.c.ling@jpl.nasa.gov

and

Wm. A. Wheaton
Infrared Processing and Analysis Center, California Institute of Technology, MS 220-06, Pasadena, CA 91125; waw@ipac.caltech.edu
Received 2004 July 18; accepted 2004 December 14

ABSTRACT

We report the results of an in-depth study of the long-term soft gamma-ray (30 keV to 1.7 MeV) flux and spectral variability of the transient source GRO J1719−24 that was first discovered by BATSE and SIGMA in the fall of 1993. Our results were obtained from the JPL BATSE-EBOP database covering a 1000 day period between 1993 January 13 and 1995 October 10. During this period, the source underwent a major outburst in the fall of 1993 when the 35–100 keV flux rose from a quiescent state of less than 16 mcrab before 1993 September 17 to a level of 1.5 crab on October 3. The source remained in this high-intensity state over the next ∼70 days, during which the 35–100 keV flux decreased monotonically by ∼33% to ∼1 crab on December 12, then decreased sharply to the pre-transition quiescent level of ∼44 mcrab on December 21, where it remained until 1994 September 5. During a 400 day period between 1994 September 5 and 1995 October 10, the source again underwent a series of five transitions when the 35–100 keV flux increased to low-intensity levels of ∼200–400 mcrab, a factor of 4–7 times lower than what was observed in 1993. The low- and high-intensity states were characterized by two different spectral shapes. The low-state spectra are described by a power law with a spectral index of ∼2. The high-state spectra, on the other hand, have two components: a thermal Comptonized shape below ∼200 keV with electron temperature kT_e of ∼37 keV and optical depth $\tau \sim 2.8$, and a soft power-law tail with photon index of ∼3.4 above 200 keV that extends to ∼500 keV. The softer high-intensity spectrum and the harder low-intensity spectrum intersect at ∼400 keV. The nonthermal power-law gamma-ray component in both the high- and low-intensity spectra suggests that the persistent nonthermal emission source is coupled to the hot and variable thermal emission source in the system. Furthermore, the correlation of the spectral characteristics with the high- and low-intensity states resembles that seen in two other gamma-ray–emitting black hole candidates, GRO J0422+32 and Cygnus X-1, suggesting that perhaps similar system configurations and processes are occurring in these systems. Possible scenarios for interpreting these behaviors are discussed.

Subject headings: black hole physics — gamma rays: observations

1. INTRODUCTION

The transient gamma-ray source GRO J1719−24 (Nova Oph 1993) was first discovered by BATSE on the *Compton Gamma Ray Observatory* (*CGRO*; Harmon et al. 1993b) and SIGMA on *Granat* (Ballet et al. 1993) on 1993 September 25 (TJD 9255, where TJD [Truncated Julian Day] = JD [Julian Day] − 2,440,000.5) when the hard X-ray (40–150 keV) flux emerged suddenly from the quiescent state of 12 mcrab (2 σ upper limit) measured by SIGMA (Revnivtsev et al. 1998), integrated over the period from 1993 August 28 to September 19 (TJD 9227–9249), to 17 mcrab on 1993 September 25–26 (TJD 9255–9256), and then to a peak level of 1.4 crab measured by BATSE (Harmon et al. 1993a) 5 days later on September 30 (TJD 9260). BATSE (Harmon et al. 1993a) then showed that the hard X-ray flux decreased gradually by ∼0.3% ± 0.05% per day for the next 2.5 months to a level of ∼1.1 crab on December 9 (TJD 9330), before dropping off sharply in the next 6 days to below the BATSE 1 day sensitivity level around December 16 (TJD 9337). The source stayed at this quiescent state until the fall of 1994, when SIGMA (Churazov et al. 1994; Revnivtsev et al. 1998) detected the hard X-ray flux again at ∼115 mcrab, ∼10% of the peak flux level observed in the fall of 1993. Strong X-ray emission was also detected by *Mir-Kvant* (Borozdin et al. 1995) on 1995 February 16 (TJD 9764) and by BATSE (Hjellming et al. 1996) in five separate episodes between 1994 September 1 (TJD 9596) and 1995 September 6 (TJD 9995), when the hard X-ray flux reached a level of ∼200–300 mcrab (see § 3 below), a factor of 3–5 lower than observed in 1993.

The optical counterpart of GRO J1719−24 was identified by Della Valle et al. (1994) and Masetti et al. (1996) as being a low-mass binary (V2293 Oph) with a periodicity of 14.7 hr. According to the optical superhump modulation analysis of Masetti et al. (1996), the system consists of a compact object of 4.9 $M_\odot$ and a companion main-sequence star of K spectral type (or later) of ∼1.6 $M_\odot$. The distance was estimated to be ∼2–2.8 kpc. When the source was in the quiescent state prior to the transition, no optical counterpart was observed at a level fainter than $V \sim 21$. During the 1993 outburst, the visual magnitude increased by ∼4.4 to $V = 16.65$. A strong QPO peak in the 20–100 keV band was observed by BATSE (van der Hooft et al. 1996) during the ∼80 day high-intensity state in 1993 with centroid frequency varying from ∼0.04 Hz at the onset of the outburst to ∼0.3 Hz at the end.

The radio counterpart was observed by the Very Large Array (VLA; Mirabel et al. 1993; Della Valle et al. 1994) during the

1993 outburst on October 5 at a position consistent with the optical counterpart. The radio compact source showed a relatively flat spectrum with flux densities of 4.6 ± 0.4 and 4.9 ± 0.2 mJy at $\lambda = 20$ and 6 cm, respectively. Radio emission was also measured by the Molonglo Observatory Synthesis Telescope (MOST) at 843 MHz and by the VLA at frequencies of 1.49, 4.9, 8.4, and 14.9 GHz during the 1994–1995 (TJD 9745–9966) period when the source underwent a series of low-level outbursts described above (Hjellming et al. 1996). Specifically, the 4.9 GHz measured by the VLA between TJD 9749 and 9800 showed a power-law decay of the light curve that matched closely the decay of one of the events observed by BATSE. This was interpreted as the radio synchrotron emission associated with the ejection of relativistic electrons from an expanding spherical shell.

Soft gamma-ray spectra of GRO J1719−24 above 30 keV between 1993 January and 1995 September were measured by both the SIGMA experiment (Revnivtsev et al. 1998) and by OSSE on *CGRO* (Grove et al. 1998). Revnivtsev et al. (1998) reported nearly contemporaneous observations with TTM on board *Mir-Kvant* and SIGMA in the composite 2–300 keV range made during seven separate periods: two during the pre-outburst period, 1993 February 17 to April 9 and 1993 August 28 to September 19; two during the rising phase (1993 September 25–28) and the plateau phase (1993 September 29 to October 14) of the 1993 outburst; and three during the post-outburst low-intensity periods, 1994 February 24 to March 25, 1994 September 1–30, and 1995 September 9–21. Grove et al. (1998) reported OSSE observations made in five separate periods, 1993 October 25–27, 1993 October 30–31, 1994 November 9–15, 1994 November 29 to December 7, and 1995 February 1–14. Both the SIGMA and OSSE results indicated possible variability between spectra obtained during the plateau phase of the flare observed in the fall of 1993 and those obtained in the fall of 1994, when the flux was significantly lower. The 1993 high-intensity spectra were generally better fitted with either the Comptonized model (Sunyaev & Titarchuk 1980), a thermal bremsstrahlung model, or an exponentially truncated power law than a power law, while the 1994 low-intensity spectra were better fitted with either a power law or a less well constrained thermal bremsstrahlung model. Grove et al. (1998) further suggested that of the seven Galactic black hole gamma-ray emitters observed by OSSE, the two spectral states observed in GRO J1719−24 most strongly resemble those seen in Cygnus X-1.

The spectral variability shown between the high- and low-intensity spectra observed by SIGMA and OSSE with limited pointed observations has important implications in our understanding of the system. It therefore needs to be confirmed and studied with all available data on the source. In this paper, we report results obtained from BATSE's nearly continuous daily monitoring of the 35–1700 keV emission of the source covering a 1000 day period between TJD 9000 and 10,000. These results, which were produced by the JPL EBOP (Enhanced BATSE Occultation Package) analysis system (Ling et al. 1996, 2000), consist of light curves in six broad energy bands, 35–100, 100–200, 200–300, 300–400, 400–700, and 700–1000 keV, and 14-channel daily spectra as well as spectra integrated over days and weeks. In this paper, we address the following questions: (1) What new information is revealed from the energy-dependent gamma-ray flux history and variability shown by this source during this period? (2) What are the characteristics of the high-intensity and the low-intensity soft gamma-ray spectra in this energy range? (3) How did the source spectrum evolve between the low- and high-intensity states? (4) How do the spectral characteristics of this source compare with other black hole candidates such as GRO J0422+32, Cygnus X-1, GRO J1655−40, and GRS 1915+105? and (5) What can we learn from the gamma-ray spectral characteristics and variability shown in these sources to better understand their system configurations and the physical processes? We address these issues in § 4. In § 2 we provide a brief description of the EBOP database and technique. Results produced by EBOP are presented in § 3.

2. EBOP DATABASE AND TECHNIQUE

EBOP, as described by Ling et al. (1996, 2000) and Ling & Wheaton (2003a, 2003b), was used to produce the results reported in this paper. We have also completed recently a high-level database with EBOP for studying the long-term flux and spectral characteristics and variations of 75 gamma-ray sources included in the present EBOP catalog covering the full 9 year *CGRO* mission from 1991 to 2000. This high-level database includes daily count-rate and photon spectra (assuming a power-law fit, or fits with a Compton model whenever it is needed, to the count-rate spectrum using XSPEC [Arnaud 1996]) and spectra integrated over each of the 315 nominal *CGRO* viewing periods (VPs) of typically 6–14 days' duration, for each of the eight BATSE large-area detectors (LADs) and for each of the 75 sources. Many terms in the background differ strongly for different LADs. The detector responses to any given source, which implicitly transform LAD count rates into photon fluxes, also differ. To reduce the possible effects of systematic errors in the results, EBOP includes a LAD flux consistency check. Days when the fluxes derived from the source-viewing LADs (typically 2–4 for each VP) are mutually inconsistent (at the 95% level) are rejected from inclusion in the results. Because some terms in the background (direct cosmic-ray effects, in particular) are correlated with the Earth-occultation periodicity, this filter on the results is not truly airtight, although logically necessary and useful. Of the 780 daily spectra covering the period between TJD 9000 and 10,000 included in this report, only two have failed the consistency test using the criteria described by Ling et al. (1996, 2000).

3. RESULTS

3.1. *Flux Histories*

The flux histories in the six broad energy bands, 35–100, 100–200, 200–300, 300–400, 400–700, and 700–1000 keV, covering the period between 1993 January 13 (TJD 9000) and 1995 October 10 (TJD 10,000) are shown in Figure 1. The resolutions are 1 day for the first two panels, 2 days for the third panel, and 5 days for the last three panels. Between TJD 9264 and 9341, *CGRO* underwent three reboost operations on TJD 9264–9279, TJD 9310–9314, and TJD 9334–9341, during which no data on the source were available, as reflected by the data gaps shown in these light curves.

Over the 1000 day period, the source underwent a series of gamma-ray flux transitions:

1. The hard X-ray (35–100 keV) flux rose sharply from the quiescent state of $(2.19 \pm 0.74) \times 10^{-5}$ photons cm^{-2} s^{-1} keV^{-1} ($\sim$10 mcrab) measured between TJD 9000 and 9247 to 114 mcrab on TJD 9249 ($\sim 2\,\sigma$), the first hint of the beginning of a transition, and then to $\sim$1.5 crab ($\sim 34\,\sigma$) 14 days later on TJD 9263. All errors associated with the measured fluxes reported in this paper are 1 σ significance.

2. The source stayed roughly in the high-intensity state for $\sim$76 days between TJD 9257 and 9333. During this period, the

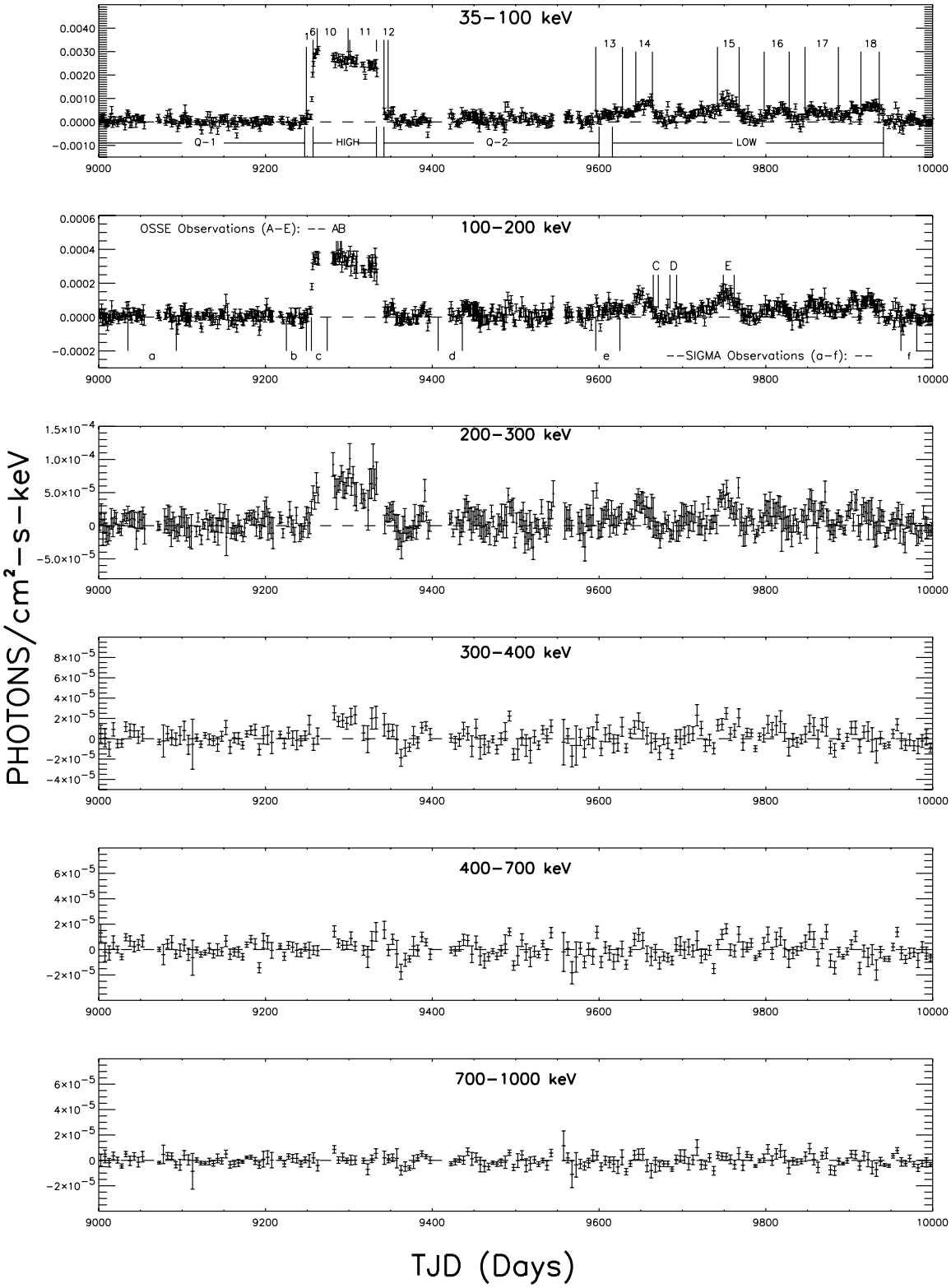

FIG. 1.—Flux histories in the six broad energy bands covering the period between 1993 January 13 (TJD 9000) and 1995 October 10 (TJD 10,000). The resolutions are 1 day in the first two panels, 2 days in the third panel, and 5 days in the last three panels. During the high-intensity period between TJD 9257 and 9333, positive gamma-ray fluxes in the six energy bands were measured at ~127, 108, 30, 9.9, 4.8, and 1.6 σ significance. Between TJD 9600 and 10,000, the source flared again five different times (marked 14, 15, 16, 17, and 18) and the 35–100 keV fluxes were measured at lower levels of ~354, ~354, ~197, ~189, and ~290 mcrab, respectively. Data gaps shown between TJD 9264 and 9341 were periods when the spacecraft underwent reboost operations. Also shown in the second panel are the markers for the six SIGMA observational periods (labeled a–f) and the five OSSE observational periods (labeled A–E).

TABLE 1
AVERAGE GAMMA-RAY FLUXES FOR THE QUIESCENT AND HIGH-INTENSITY SPECTRAL STATES

Energy (keV)	Crab Flux[a]	Quiescent Period 1[b]	High-State Period[c]	Quiescent Period 2[d]
35–100	$(208.6 \pm 0.3) \times 10^{-5}$	$(2.19 \pm 0.74) \times 10^{-5}$	$(257.34 \pm 2.04) \times 10^{-5}$	$(9.28 \pm 0.88) \times 10^{-5}$
100–200	$(30.66 \pm 0.06) \times 10^{-5}$	$(1.92 \pm 1.51) \times 10^{-6}$	$(32.30 \pm 0.46) \times 10^{-5}$	$(1.43 \pm 0.19) \times 10^{-5}$
200–300	$(9.20 \pm 0.03) \times 10^{-5}$	$(1.66 \pm 0.96) \times 10^{-6}$	$(5.98 \pm 0.30) \times 10^{-5}$	$(3.30 \pm 1.18) \times 10^{-6}$
300–400	$(3.71 \pm 0.03) \times 10^{-5}$	$(5.61 \pm 7.62) \times 10^{-7}$	$(1.65 \pm 0.23) \times 10^{-5}$	$(9.68 \pm 9.44) \times 10^{-7}$
400–700	$(14.88 \pm 0.24) \times 10^{-6}$	$(1.60 \pm 4.89) \times 10^{-7}$	$(4.12 \pm 1.29) \times 10^{-6}$	$(1.05 \pm 6.05) \times 10^{-7}$
700–1000	$(5.44 \pm 0.17) \times 10^{-6}$	$(-1.65 \pm 3.24) \times 10^{-7}$	$(1.00 \pm 0.89) \times 10^{-6}$	$(-5.40 \pm 4.09) \times 10^{-7}$

NOTE.—All flux values are given in units of photons cm^{-2} s^{-1} keV^{-1}.
[a] Ling & Wheaton (2003b).
[b] TJD 9000–9247; 186 day integration.
[c] TJD 9262–9333; 42 day integration.
[d] TJD 9342–9600; 182 day integration.

35–100 keV flux decreased gradually from its peak value on TJD 9263 of 1.5 crab to ~1 crab on TJD 9333 before the third reboost. When we observed the source again at the other end of the reboost on TJD 9342, the source flux returned roughly to the preflare level. The averaged 35–100 keV flux over the next ~260 days from TJD 9342 to 9600 was $(9.28 \pm 0.88) \times 10^{-5}$ photons cm^{-2} s^{-1} keV^{-1} (~44 mcrab).

3. During the high-intensity period between TJD 9262 and 9333, BATSE observed high-energy gamma-ray fluxes up to ~400–700 keV at a level of $(4.12 \pm 1.29) \times 10^{-6}$ photons cm^{-2} s^{-1} keV^{-1} (~0.28 crab). Table 1 lists the average fluxes measured in the six energy bins during the high-intensity period as well as the quiescent periods before and after the outburst. The average 35–100 keV flux measured during the high state was ~1.2 crab at a level of $(2.57 \pm 0.02) \times 10^{-3}$ photons cm^{-2} s^{-1} keV^{-1}.

4. During the 400 day period between TJD 9600 and 10,000, the source flared again five different times (marked 14, 15, 16, 17, and 18 in the first panel of Fig. 1), but to levels significantly lower than the high-state level. The average 35–100 keV flux levels measured in these five periods are $(7.38 \pm 0.27) \times 10^{-4}$ (~354 mcrab), $(7.40 \pm 0.27) \times 10^{-4}$ (~354 mcrab), $(4.12 \pm 0.26) \times 10^{-4}$ (~197 mcrab), $(3.95 \pm 0.21) \times 10^{-4}$ (~189 mcrab), and $(6.05 \pm 0.31) \times 10^{-4}$ (~290 mcrab) photons cm^{-2} s^{-1} keV^{-1}, respectively. Gamma-ray fluxes for the six broadband energy bins for each of these five periods are summarized in Table 2.

5. During this entire 1000 day period, GRO J1719−24 was also observed in six separate periods of various duration by SIGMA (Revnivtsev et al. 1998) and five times by OSSE (Grove et al. 1998). These are identified as a–f and A–E, respectively, in the second panel of Figure 1. We include these results for the purpose of comparing them with the BATSE results in the context of the source's long-term flux and spectral variability observed by BATSE. Specifically, the BATSE data as well as those obtained by SIGMA and OSSE are essentially the world's only available data on this source for shedding light on the high-energy processes as well as, possibly, its system configuration as revealed by the gamma-ray data.

3.2. *Spectra*

The key questions we address in this section are, what are the basic spectral characteristics associated with the various gamma-ray states, and how do they evolve as the source undergoes transitions among these states?

1. Figure 2*a* shows nine daily spectra measured between TJD 9249 and 9260 during the rising phase of the 1993 source transition from the quiescent state to the high state. In each panel, the solid line is the best-fit model to the spectral data measured by all the source-viewing LADs listed in Table 3. Pertinent information on the model fit (e.g., best-fit parameters with 1 σ error), as well as reduced χ^2 values (χ^2/degrees of freedom), is also displayed in each panel and listed in Table 3.

TABLE 2
AVERAGE GAMMA-RAY FLUXES FOR THE FIVE LOW-INTENSITY SPECTRAL STATES

Energy (keV)	Low-State Period				
	14[a]	15[b]	16[c]	17[d]	18[e]
35–100	$(73.83 \pm 2.65) \times 10^{-5}$	$(73.96 \pm 2.63) \times 10^{-5}$	$(41.22 \pm 2.55) \times 10^{-5}$	$(39.46 \pm 2.13) \times 10^{-5}$	$(60.53 \pm 3.06) \times 10^{-5}$
100–200	$(9.97 \pm 0.61) \times 10^{-5}$	$(11.28 \pm 0.51) \times 10^{-5}$	$(4.92 \pm 0.55) \times 10^{-5}$	$(5.88 \pm 0.46) \times 10^{-5}$	$(7.99 \pm 0.66) \times 10^{-5}$
200–300	$(2.86 \pm 0.45) \times 10^{-5}$	$(3.61 \pm 0.31) \times 10^{-5}$	$(1.52 \pm 0.42) \times 10^{-5}$	$(1.20 \pm 0.29) \times 10^{-5}$	$(1.29 \pm 0.50) \times 10^{-5}$
300–400	$(0.77 \pm 0.41) \times 10^{-5}$	$(1.49 \pm 0.26) \times 10^{-5}$	$(0.80 \pm 0.35) \times 10^{-5}$	$(0.31 \pm 0.26) \times 10^{-5}$	$(0.17 \pm 0.42) \times 10^{-5}$
400–700	$(0.43 \pm 0.29) \times 10^{-5}$	$(0.81 \pm 0.18) \times 10^{-5}$	$(0.39 \pm 0.24) \times 10^{-5}$	$(0.03 \pm 0.18) \times 10^{-5}$	$(-0.53 \pm 0.31) \times 10^{-5}$
700–1000	$(0.10 \pm 0.23) \times 10^{-5}$	$(0.25 \pm 0.13) \times 10^{-5}$	$(0.34 \pm 0.17) \times 10^{-5}$	$(-0.04 \pm 0.13) \times 10^{-5}$	$(-0.13 \pm 0.22) \times 10^{-5}$

NOTE.—All flux values are given in units of photons cm^{-2} s^{-1} keV^{-1}.
[a] TJD 9644–9664; 19 day integration.
[b] TJD 9742–9768; 26 day integration.
[c] TJD 9798–9828; 28 day integration.
[d] TJD 9847–9887; 38 day integration.
[e] TJD 9914–9936; 22 day integration.

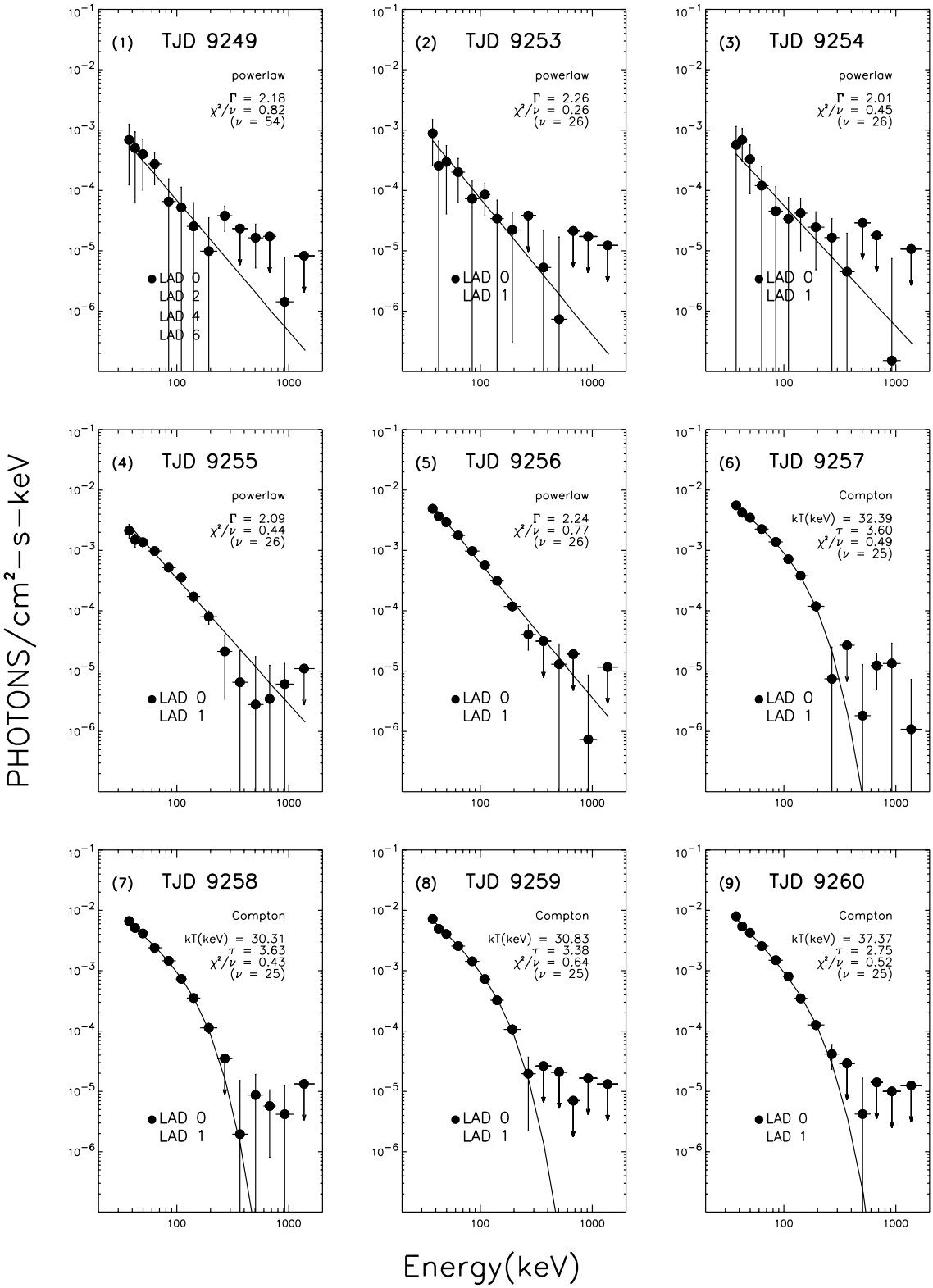

FIG. 2*a*

FIG. 2.—(*a*) Nine daily spectra measured from TJD 9249 to 9260 during the rising phase of the source transition from the quiescent state to the high state. In each panel, the solid line is the best-fit model to the spectral data measured by the source-viewing LADs. Pertinent information of the model fit is also displayed in each panel and listed in Table 3. The spectrum changed from a power-law shape prior to TJD 9256 (panels 1–5) to a Comptonized shape below 200 keV on TJD 9257 (panel 6) and stayed in this shape for the rest of the rising phase (panels 7–9). (*b*) The two averaged high-state spectra integrated over TJD 9262–9299 and TJD 9301–9333 (panels 10 and 11) can be described as having two components: a Comptonized shape below ∼200 keV and a soft power-law tail above ∼200 keV that extends to ∼400–500 keV. The seven low-state spectra measured in 1994–1995, on the other hand, have a power-law shape with photon indices of ∼2.1–2.4.

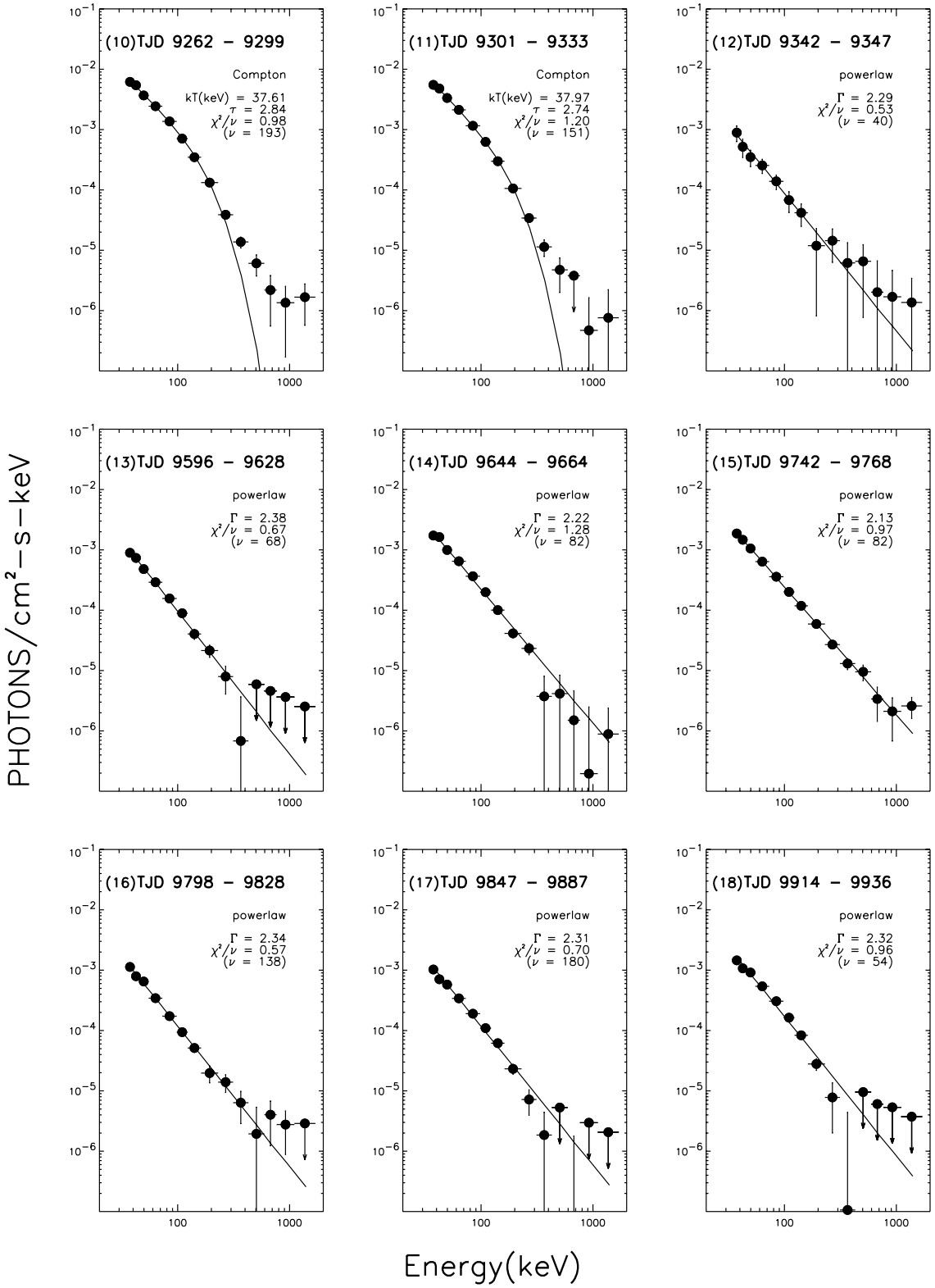

FIG. 2*b*

Because of the limited statistics of the data, the first five spectra measured between TJD 9249 and 9256 can be adequately fitted with either the power-law or the thermal Comptonization model (Sunyaev & Titarchuk 1980). However, on TJD 9257, the spectrum has a distinctly thermal Comptonized shape, and the simple power law can no longer fit the data well. Since the integrated 35–500 keV flux changed by only ∼18% from ∼932 mcrab on TJD 9256 to ∼1.1 crab on TJD 9257, a reasonable question may be raised: "Was there a definitive spectral change from either a nonthermal power-law shape or a thermal Comptonized shape seen prior to TJD 9257 to the thermal Comptonization shape on TJD 9257 and beyond?" Such a change could reflect an intrinsic

TABLE 3

BEST-FIT MODEL PARAMETERS

								POWER-LAW MODEL ($AE^{-\Gamma}$)			COMPTON MODEL (ST)			
SPECTRAL NUMBER	SPECTRAL STATE[a]	TJD	VP	DAYS OF INTEGRATION	LAD	35–100 keV FLUX[b]	HARDNESS RATIO[c]	Γ	dof	χ^2/dof	kT (keV)	τ	dof	χ^2/dof
1	RP	9249	302.3	1	0, 2, 4, 6	2.38 ± 1.19	$(1.34 \pm 1.21) \times 10^{-1}$	2.18 ± 0.48	26	0.82	...	...	...	...
2	RP	9253	303.2	1	0, 1	2.17 ± 1.11	$(0.69 \pm 1.03) \times 10^{-1}$	2.26 ± 0.63	26	0.26	69.5 ± 170.2	1.74 ± 4.64	25	0.27
3	RP	9254	303.2	1	0, 1	2.06 ± 1.04	$(1.48 \pm 1.20) \times 10^{-1}$	2.01 ± 0.72	26	0.45	81.0 ± 183.0	2.25 ± 4.76	25	0.44
4	RP	9255	303.2	1	0, 1	9.71 ± 1.03	$(8.68 \pm 2.16) \times 10^{-2}$	2.09 ± 0.12	26	0.44	43.0 ± 12.5	3.15 ± 0.98	25	0.2
5	RP	9256	303.2	1	0, 1	20.12 ± 1.04	$(7.21 \pm 1.08) \times 10^{-2}$	2.24 ± 0.07	26	0.77	43.8 ± 7.9	2.70 ± 0.53	25	0.15
6	RP	9257	303.2	1	0, 1	24.75 ± 1.01	$(5.07 \pm 0.86) \times 10^{-2}$	2.32 ± 0.06	26	2.29	32.4 ± 3.8	3.60 ± 0.53	25	0.49
7	RP	9258	303.2	1	0, 1	28.20 ± 1.04	$(4.09 \pm 0.78) \times 10^{-2}$	2.39 ± 0.06	26	2.15	30.3 ± 3.3	3.63 ± 0.55	25	0.43
8	RP	9259	303.2	1	0, 1	28.45 ± 1.03	$(4.36 \pm 0.77) \times 10^{-2}$	2.46 ± 0.06	26	2.36	30.8 ± 3.5	3.38 ± 0.50	25	0.64
9	RP	9260	303.2	1	0, 1	30.04 ± 1.03	$(5.27 \pm 0.75) \times 10^{-2}$	2.40 ± 0.05	26	1.78	37.4 ± 5.4	2.75 ± 0.39	25	0.52
10	HS	9262–9299	...	20	...	27.15 ± 0.28	$(5.97 \pm 0.23) \times 10^{-2}$	2.38 ± 0.01	194	2.61	37.6 ± 1.4	2.84 ± 0.12	193	0.98
...		9262–9263	303.4	...	0, 4	...	...	...	...	...	...	...	...	...
...		9280–9284	304	...	0, 1, 2, 3	...	...	...	...	...	...	...	...	...
...		9286–9292	305	...	0, 1, 2, 3	...	...	...	...	...	...	...	...	...
...		9294–9299	306	...	0, 1, 2, 3	...	...	...	...	...	...	...	...	...
11	HS	9301–9333	...	26	...	24.14 ± 0.26	$(5.55 \pm 0.27) \times 10^{-2}$	2.38 ± 0.02	152	2.62	38.0 ± 1.7	2.74 ± 0.13	151	1.2
...		9301–9306	307	...	0, 1, 2, 3	...	...	...	...	...	...	...	...	...
...		9308–9309	308	...	0, 1	...	...	...	...	...	...	...	...	...
...		9317-9320	308.6	...	0, 1	...	...	...	...	...	...	...	...	...
...		9323–9333	310	...	1, 3, 7	...	...	...	...	...	...	...	...	...
12	LS	9342–9347	312	6	0, 1, 2	2.84 ± 0.50	$(8.21 \pm 4.00) \times 10^{-2}$	2.29 ± 0.24	40	0.53	170.4 ± 639.9	0.70 ± 2.82	151	0.56
13	LS	9596–9628	...	22	...	3.48 ± 0.21	$(7.42 \pm 1.51) \times 10^{-2}$	2.38 ± 0.08	68	0.67	61.4 ± 26.1	1.75 ± 0.68	151	0.6
...		9596–9614	338.5	...	2, 3, 7	...	...	...	...	...	...	...	...	...
...		9616–9628	339	...	0, 4	...	...	...	...	...	...	...	...	...
14	LS	9644–9664	...	...	...	7.38 ± 0.27	$(7.81 \pm 0.95) \times 10^{-2}$	2.22 ± 0.05	82	1.28	57.6 ± 12.1	2.00 ± 0.39	151	1.2
...		9644–9649	402	...	2, 6	...	...	...	...	...	...	...	...	...
...		9651–9656	402.5	...	0, 2	...	...	...	...	...	...	...	...	...
...		9658–9664	403	...	0, 1	...	...	...	...	...	...	...	...	...
15	LS	9742–9768	...	26	...	7.40 ± 0.26	$(9.86 \pm 0.71) \times 10^{-2}$	2.13 ± 0.048	82	0.97	125.1 ± 33.9	1.11 ± 0.32	151	1.06
...		9742–9761	410	...	0, 1, 2, 3	...	...	...	...	...	...	...	...	...
...		9763–9768	411.1	...	3, 7	...	...	...	...	...	...	...	...	...
16	LS	9798–9828	...	28	...	4.12 ± 0.26	$(6.74 \pm 1.57) \times 10^{-2}$	2.34 ± 0.09	138	0.57	103.9 ± 78.2	1.08 ± 0.86	151	0.59
...		9798–9804	414	...	0, 4, 5	...	...	...	...	...	...	...	...	...
...		9806–9810	414.3	...	0, 2, 4	...	...	...	...	...	...	...	...	...
...		9812–9817	419.1	...	1, 5	...	...	...	...	...	...	...	...	...
...		9819–9828	415	...	4, 5	...	...	...	...	...	...	...	...	...
17	LS	9847–9887	...	38	...	3.95 ± 0.21	$(7.12 \pm 1.14) \times 10^{-2}$	2.31 ± 0.07	180	0.7	51.2 ± 11.9	2.24 ± 0.51	151	0.63
...		9847–9859	419	...	5, 7	...	...	...	...	...	...	...	...	...
...		9861–9873	420	...	1, 5, 7	...	...	...	...	...	...	...	...	...
...		9875–9880	421	...	0, 2, 4, 6	...	...	...	...	...	...	...	...	...
...		9882–9887	422	...	0, 2, 4, 6	...	...	...	...	...	...	...	...	...
18	LS	9914–9936	...	22	...	6.05 ± 0.31	$(5.47 \pm 1.16) \times 10^{-2}$	2.32 ± 0.06	54	0.96	37.4 ± 6.3	2.95 ± 0.55	151	0.58
...		9914–9922	424	...	4, 6	...	...	...	...	...	...	...	...	...
...		9924–9936	425	...	5, 7	...	...	...	...	...	...	...	...	...

[a] RP = rising phase; HS = high state; LS = low state.

[b] In units of 10^{-4} photons cm^{-2} s^{-1} keV^{-1}.

[c] HR = (150–300 keV flux)/(35–150 keV flux).

change of the physical conditions of the system and needs to be understood. In addressing this question, we examine the hardness ratio (HR) of the spectra, where HR = (150–300 keV flux)/(35–150 keV flux) (see Table 3). We then use the HR to characterize the broad spectral shape of the low- and high-intensity spectra measured both during the 1993 transition (Fig. 2*a*, panels 1–9, and Fig. 2*b*, panels 10–11) and in 1994–1995 (Fig. 2*b*, panels 12–18). For TJD 9255 and 9256, the HRs were measured at $(8.68 \pm 2.16)\times10^{-2}$ and $(7.21 \pm 1.08)\times10^{-2}$, respectively. The weighted average of the two values is $(7.58 \pm 0.96)\times10^{-2}$. This is compared to $(5.07 \pm 0.86)\times10^{-2}$ for the TJD 9257 spectrum. The difference is significant at the $\sim2\,\sigma$ level. Since the average HR of $(7.58 \pm 0.96)\times10^{-2}$ measured on TJD 9255 and 9256 is consistent with the average HR of the seven low-intensity power-law spectra measured in 1994–1995 (Fig. 2*b*, panels 12–18) of $(7.96 \pm 0.39)\times10^{-2}$, these results suggest that the source spectrum changed from a power-law to a thermal Comptonization shape within 1 day from TJD 9256 to 9257 during the rising phase of the 1993 transition.

2. The source spectrum remained in this same Comptonized shape for the rest of the rising phase (Fig. 2*a*, panels 6–9) from TJD 9257 to 9260 and when the source was in the high-intensity state from TJD 9262 to 9333 (Fig. 2*b*, panels 10–11). The weighted average of the HR of these six spectra is $(5.61 \pm 0.16)\times10^{-2}$.

3. The two averaged high-state spectra with improved statistics integrated over TJD 9262–9299 and TJD 9301–9333 (Fig. 2*b*, panels 10 and 11), and their combined spectrum shown in Figure 3 specifically, showed two components: a soft power-law tail of photon index 3.37 above 200 keV, which extended to ~500 keV, superposed on a low-energy Comptonized component below 200 keV. Because the declining phase from the high state to the quiescent state occurred during the period of the reboost of the *CGRO* spacecraft, no information on the temporal structure of the decline, date, and flux threshold at which the spectrum underwent changes was obtained.

4. In contrast to the two-component high-state spectrum described above, the seven time-averaged low-state spectra shown in Figure 2*b* (panels 12–18) are all consistent with a single power law with photon indices of ~2.1–2.4. A comparison of a typical low-state spectrum (Fig. 2*b*, panel 15) with the high-state spectrum is shown in Figure 3. In the soft gamma-ray region above 200 keV, the spectrum of the low-intensity state is harder while that of the high-intensity is softer. The two spectra intersect at ~400 keV.

5. Table 3 lists the best-fit parameters of two contrasting models, namely, a nonthermal power-law model and a thermal Comptonization model (Sunyaev & Titarchuk 1980), to each of the 18 spectra shown in Figures 2*a* and 2*b*. The thermal Comptonization model fits the high-state spectra (panels 6–11) well, but not the power law. However, for the low-intensity state spectra (panels 12–18), while both the power-law and Compton models fit the spectra adequately, the power-law model is generally preferred because its model parameters are better constrained compared to those of the Compton models, as indicated by the size of the errors.

6. The basic features of the high- and low-intensity spectra described above were generally consistent with those observed by SIGMA (Revnivtsev et al. 1998) and OSSE (Grove et al. 1998). Namely, the high-intensity state spectra were better characterized by either the Compton model (Revnivtsev et al. 1998) or an exponential truncated power law (Grove et al. 1998), and the low-intensity spectra were better fitted with a power law. Tables 4, 5, and 6 compare the best-fit model parameters measured by BATSE-EBOP with nearly contemporaneous results reported by SIGMA (Table 4) and OSSE (Tables 5 and 6). BATSE results generally agree well with those of SIGMA when contemporaneous measurements are directly compared. There is only one case when the comparison is not as good. This is during the period of SIGMA observations between TJD 9259 and 9274 (1993 September 29 to October 14) when BATSE collected no data during 11 days of this 16 day period, from TJD 9264 to 9274, because of *CGRO* reboost operations. BATSE and OSSE results also showed good agreement for one of the two periods when nearly contemporaneous measurements can be directly compared (e.g., TJD 9665–9671; see Table 5). However, for the second spectrum that includes OSSE observations A, B, and E (see Fig. 1, second panel), Grove et al. (1998) stated that the spectrum measured during period E between 1995 February 1 and 14 (TJD 9749–9762) was better fitted with the exponential truncated power law model than the power-law model, similar to the spectra measured in periods A and B. Consequently, they combined the three spectra and obtained the best-fit parameters for the combined spectrum (see Table 5). BATSE results showed that neither model fits the combined spectrum well. While both a power law and an exponential truncated power law fit the period E data adequately (see Table 6), the best-fit parameters of these two models are consistent with a single power law with photon index of ~2.1–2.2. On the other hand, the 4 day BATSE spectrum measured nearly

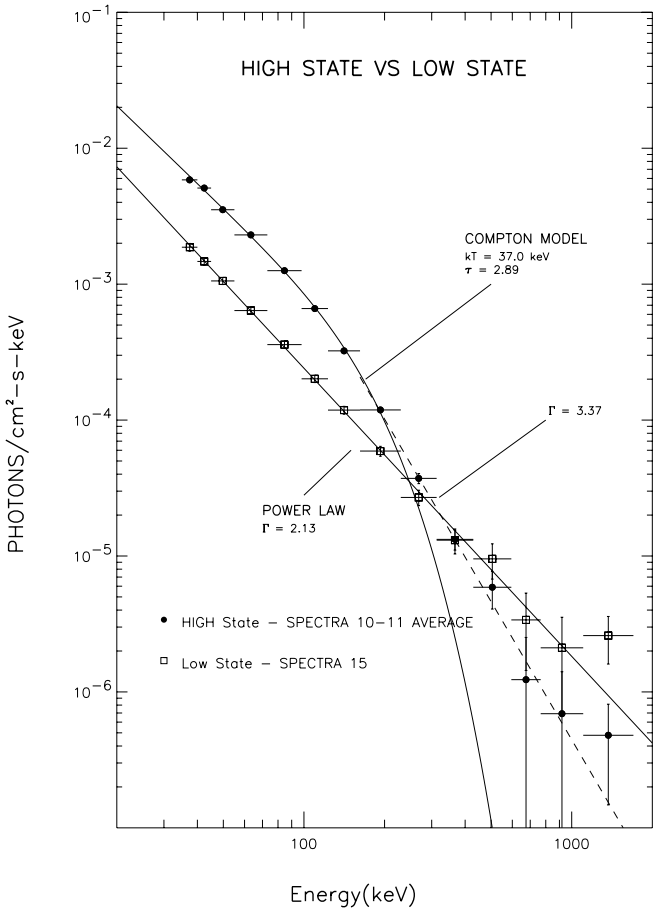

FIG. 3.—Comparison of a typical low-state (Fig. 2*b*, panel 15) spectrum with the average of the two high-state spectra shown in Fig. 2*b*, panels 10 and 11. The high- and low-state spectra intersect at ~400 keV, compared to those observed for GRO J0422+32 at ~600 keV (Ling & Wheaton 2003a) and Cygnus X-1 at ~1 MeV (Ling & Wheaton 2005; McConnell et al. 2002).

TABLE 4

COMPARISON OF BEST-FIT MODEL PARAMETERS OF CONTEMPORANEOUS MEASUREMENTS BETWEEN BATSE AND SIGMA

			POWER LAW ($\sim E^{-\Gamma}$)		COMPTON MODEL		
INSTRUMENT	DATES	TJD	Γ	χ^2(dof)	kT (keV)	τ	χ^2(dof)
First period:							
SIGMA	1993 Sep 25–26	9255–9256	2.00 ± 0.07	76.0(57)	55^{+33}_{-10}	$2.4^{+0.6}_{-0.7}$	73(56)
BATSE	1993 Sep 25–26	9255–9256	2.19 ± 0.06	106.8(54)	45.7 ± 8.3	2.69 ± 0.46	85.7(53)
Second period:							
SIGMA	1993 Sep 26–28	9256–9258	2.33 ± 0.05	88.2(57)	37^{+6}_{-4}	2.7 ± 04	66(56)
BATSE	1993 Sep 26–28	9256–9258	2.33 ± 0.03	172.3(82)	33.9 ± 2.4	3.37 ± 0.31	71.5(81)
Third period:							
SIGMA	1993 Sep 29–Oct 14	9259–9274	2.34 ± 0.01	430.8(57)	$42.6^{+1.4}_{-1.3}$	2.3 ± 0.1	90(56)
BATSE	1993 Sep 29–30, 1993 Oct 2–3	9259–9260, 9262–9263	2.44 ± 0.03	212.8(109)	32.6 ± 2.1	3.15 ± 0.23	64.1(109)
Fourth period:							
SIGMA	1994 Sep 1–30	9596–9625	2.19 ± 0.15	60(57)	$68^{+\infty}_{-28}$	1.7 ± 1.2	59(56)
BATSE	1994 Sep 1–19, 1994 Sep 21–30	9596–9614, 9616–9625	2.38 ± 0.08	45.5(68)	61.4 ± 26.1	1.75 ± 0.68	40.3(68)

TABLE 5

COMPARISON OF BEST-FIT MODEL PARAMETERS OF CONTEMPORANEOUS MEASUREMENTS BETWEEN BATSE AND OSSE

			POWER LAW ($\sim E^{-\Gamma}$)		EXPONENTIAL TRUNCATED POWER LAW ($\sim E^{-\Gamma} e^{-E/E_f}$)		
INSTRUMENT	DATES	TJD	Γ	χ^2(dof)	Γ	E_f (keV)	χ^2(dof)
OSSE A, B, E	1993 Oct 25–27, 1993 Oct 30–31, 1995 Feb 1–14	9285–9287, 9290–9291, 9749–9762	...	...	1.53 ± 0.06	115 ± 8	Not available
BATSE A, B, E	1993 Oct 26–27, 1993 Oct 30–31, 1995 Feb 1–13	9286–9287, 9290–9291, 9749–9762	2.26 ± 0.02	1007(110)	1.71 ± 0.13	197.2 ± 47.4	985(109)
OSSE C	1994 Nov 9–15	9665–9671	2.42 ± 0.08	Not available	...	...	...
BATSE	1994 Nov 10–15	9666–9670	2.51 ± 0.10	33.5(26)	...	...	...

TABLE 6

BEST-FIT MODEL PARAMETERS OF THE BATSE SPECTRUM MEASURED DURING THE THREE OSSE OBSERVATIONAL PERIODS A, B, AND E

			POWER LAW ($\sim E^{-\Gamma}$)		EXPONENTIAL TRUNCATED POWER LAW ($\sim E^{-\Gamma} e^{-E/E_f}$)		
PERIOD	DATES	TJD	Γ	χ^2(dof)	Γ	E_f (keV)	χ^2(dof)
A, B	1993 Oct 26–27, 1993 Oct 30–31	9286–9287, 9290–9291	2.36 ± 0.03	238.2(222)	1.24 ± 0.16	88.0 ± 14.5	164.5(221)
E	1995 Feb 1–13	9749-9761	2.19 ± 0.08	35.4(54)	2.11 ± 0.131	1472.7 ± 2546.0	35.1(53)

contemporaneously with OSSE periods A and B showed a slightly better fit with the exponential truncated power law than the power law (Table 6).

4. DISCUSSION

GRO J1719−24, a low-mass X-ray binary system with a 14.7 hr periodicity, consisting of a $\sim$4.9 $M_\odot$ compact object and a $\sim$1.6 $M_\odot$ companion star (Della Valle et al. 1994; Masetti et al. 1996), is one of three Galactic black hole systems, along with GRO J0422+32 (Ling & Wheaton 2003a) and Cygnus X-1 (Phlips et al. 1996; Ling et al. 1997; McConnell et al. 2000, 2002), that displayed similar gamma-ray spectral characteristics when undergoing transitions between the high and low gamma-ray intensity states (Ling & Wheaton 2005):

1. When these sources were in the high gamma-ray intensity state (γ_2 for Cygnus X-1; Ling et al. 1997), their spectra showed two components: a Comptonized component from $\sim$30 to $\sim$200 keV followed by a soft power-law tail of photon index >3 above $\sim$200 keV that extended to $\sim$500 keV for GRO J1719−24, $\sim$1 MeV for Cygnus X-1 (Ling et al. 1997; McConnell et al. 2000), and $\sim$600 keV for GRO J0422+32 (Ling & Wheaton 2003a). For GRO J1719−24, the 35–200 keV emission was likely to be produced by Compton scattering off hot electrons in the system with electron temperature kT_e of $\sim$37 keV and optical depth τ of $\sim$2.9.

2. When these sources were in the low gamma-ray intensity state (γ_0 for Cygnus X-1; Ling et al. 1997), the Comptonized spectral shape below $\sim$200–300 keV vanished. The entire spectrum from 30 keV to $\sim$1.5 MeV was consistent with a power law with a photon index of $\sim$2.1–2.4 for GRO J1719−24. This is compared to $\sim$1.8–2.1 for GRO J0422+32 (Ling & Wheaton 2003a) and $\sim$2.6–2.7 for Cygnus X-1 (Phlips et al. 1996; Ling et al. 1997). Because the low-intensity spectrum is harder than the high-intensity spectrum above $\sim$200 keV, the two spectra intersect at $\sim$400 keV for GRO J1719−24. This is compared to $\sim$600 keV for GRO J0422+32 (Ling & Wheaton 2003a) and $\sim$1 MeV for Cygnus X-1 (Ling & Wheaton 2005; McConnell et al. 2002).

3. There is some weak evidence ($\sim$2 σ) that the spectrum changed from a power-law shape on TJD 9256 to a thermal Comptonized shape on TJD 9257 during the rising phase of the 1993 transition. This suggests that the system has undergone a change in its configuration and that the timescale for such a change could be on the order of 1 day. Because of the reboost operation, no similar information was obtained during the declining phase of the event $\sim$80 days later.

4. The high gamma-ray intensity state (γ_2) for Cygnus X-1 was generally referred as the low/hard state, while the low gamma-ray intensity state (γ_0) was referred to as the high/soft state, a description derived from the intensity and spectral shape of the 1–10 keV emission. We would like to point out that such labels are quite misleading in terms of gamma-ray emission. In the gamma-ray region between 30 keV and 1 MeV, the intensity is higher and the spectrum is softer above $\sim$200 keV for the so-called low/hard X-ray state compared to the lower intensity and harder spectrum for the high/soft X-ray state. In order to prevent any unnecessary confusion in our discussion of the gamma-ray spectral features of these black hole systems, we have avoided using these standard labels that have been used in the past for describing the X-ray spectrum. We suggest that any future work using these identifiers should specify the spectral region that they refer to.

5. The two-component characteristic of the high-intensity state spectra, namely a thermal component below $\sim$200 keV and a nonthermal component above 200 keV, shown in these three sources is different from the pure simple power-law spectrum shown in GRO J1655−40 (Grove et al. 1998; Case et al. 2005) and the broken power law shown in GRS 1915+105 (Case et al. 2005), two other black hole systems that are generally considered to be microquasars. These results confirm previous observations (Grove et al. 1998) that there are at least two classes of gamma-ray–emitting black hole candidates in our Galaxy.

The evidence for a persistent power-law component in both the high- and low-intensity spectra of GRO J1719−24 strongly suggests the presence of nonthermal processes in the system in both the high- and low-intensity situations. The strong similarity of the gamma-ray characteristics shown in GRO J1719−24 on one hand and Cygnus X-1 and GRO J0422+32 on the other raises the following key questions that need to be addressed: (1) What is the basic system configuration for interpreting the gamma-ray spectra? and (2) What are the physical processes responsible for the changes of the spectral shapes shown between the high- and low-intensity spectra?

Over the past several years, a number of theories have been advanced in explaining the thermal and nonthermal emission observed in the high-intensity state spectra. Chakrabarti & Titarchuk (1995) and Turolla et al. (2002) have proposed that relativistic electrons with energies up to 1 MeV may be associated with free infall of matter onto the black hole in the converging flow region near the event horizon. The observed power-law spectral tail may possibly be produced by Compton upscattering of photons produced in the system off these infalling electrons. Meier (2001) suggested that nonthermal gamma-ray emission may be associated with jets, which he claimed is a natural consequence of accretion flows onto rotating black holes. More recently, the magnetically dominated accretion flow (MDAF) model of D. L. Meier (2004, private communication) further develops the idea and integrates accretion and jet production as an extension of the ADAF (Esin et al. 1998) and Shakura & Sunyaev (1976) disk models. There were also suggestions for a hybrid thermal/nonthermal Comptonization model (Coppi 1999; Gierlinski et al. 1999). In this model, the electron distribution consisted of two components, a Maxwellian component with a temperature kT plus a nonthermal power-law component. The acceleration of nonthermal electrons is independently taking place but is coupled to the background thermal plasma by Compton scattering and Coulomb collision processes. While such a model aimed to explain the two-component high-intensity gamma-ray spectra observed in black hole binary systems such as GRO J1719−24, GRO J0422+32, and Cygnus X-1, no attempts have been made to explain how the spectrum evolved into a power law in the low-intensity scenario.

Ling & Wheaton (2003a) suggested a possible system scenario for explaining both the high- and low-intensity spectra. It is based on the ADAF model of Esin et al. (1998), along with the source geometry envisioned by Poutanen & Coppi (1998) and others. Because the nonthermal power law was fully visible in the 35 keV to 1 MeV low-intensity spectrum, while only partially visible above 200 keV, and fully hidden behind the Comptonized spectrum below 200 keV in the high-intensity spectrum, they proposed a system for the high-intensity scenario that consists of a hot inner corona, a cooler outer thin disk, and a separate region that produces the power-law gamma-ray emission. We hereby refer to the latter as the ''nonthermal

emission region'' (NTER). The NTER may include a jet (see Ling & Wheaton 2003a, Fig. 6; Ling & Wheaton 2005) and possibly also the converging flow region discussed above. Under such conditions, the transition radius of the disk is $\sim$100 Schwarzschild radii from the black hole. Electrons in the hot corona upscatter the low-energy photons produced both inside the corona and in the outer disk to form the Comptonized component that dominates the spectrum in the 35–200 keV range. These same electrons also downscatter the high-energy photons (>10 MeV) produced in the NTER, resulting in the formation of a softer power-law component observed in the 200 keV to 1 MeV range. Under the low-intensity scenario that could be triggered by a significant increase in the accretion rate, a large quantity of soft photons was produced in the disk that cooled and quenched the hot corona and moved the transition radius inward to a distance very close to the horizon. Under this condition, the Comptonized component below 200 keV disappeared and the entire 35–1000 keV spectrum is dominated by the unperturbed emission produced by the NTER.

In summary, similar gamma-ray spectral characteristics and evolutions between high- and low-intensity transitions have now been observed in three Galactic binary black hole systems: GRO J1719−24, GRO J0422+32, and Cygnus X-1. These results present new challenges and constraints to future theoretical work in this field. We hope this work will stimulate a renewed interest in modelers to effectively address the questions posed by the new results presented in this paper.

We wish to thank Gerald Fishman and his BATSE team for their support of the BATSE Earth Occultation investigation effort at JPL throughout the years; Dave Meier, Michael Cherry, and Gary Case for their useful comments on this manuscript; and undergraduate students Robert Kern, Zachary Medin, and Juan Estrella for processing the data. The work described in this paper was carried out at the Jet Propulsion Laboratory, California Institute of Technology, under contract with the National Aeronautics and Space Administration.

REFERENCES

Arnaud, K. A. 1996, in ASP Conf. Ser. 101, Astronomical Data Analysis Software and Systems V, ed. G. Jacoby & J. Barnes (San Francisco: ASP), 17
Ballet, J., Denis, M., Gilfanov, M., & Sunyaev, R. 1993, IAU Circ., 5874, 1
Borozdin, K., Alexandrovich, N., & Sunyaev, R. 1995, IAU Circ., 6141, 2
Case, G. L., Cherry, M. L., Fannin, C., Rodi, J., Ling, J. C., & Wheaton, Wm. A. 2005, Chinese J. Astron. Astrophys., in press (astro-ph/0409306)
Chakrabarti, S. K., & Titarchuk, L. 1995, ApJ, 455, 623
Churazov, E., Gilfanov, M., Ballet, J., & Jourdain, E. 1994, IAU Circ., 6083, 2
Coppi, P. S. 1999, in ASP Conf. Ser. 161, High Energy Processes in Accreting Black Holes, ed. J. Poutanen & R. Svensson (San Francisco: ASP), 375
Della Valle, M., Mirabel, F., & Rodriguez, L. F. 1994, A&A, 290, 803
Esin, A. A., Narayan, R., Cui, W., Grove, J. E., & Zhang, S. 1998, ApJ, 505, 854
Gierlinski, M., Zdziarski, A. A., Poutanen, J., Coppi, P. S., Ebisawa, K., & Johnson, W. N. 1999, MNRAS, 309, 496
Grove, J. E., Johnson, W. N., Kroeger, R. A., McNaron-Brown, K., & Skibo, J. G. 1998, ApJ, 500, 899
Harmon, B. A., Fishman, G. J., Paciesas, W. S., & Zhang, S. N. 1993a, IAU Circ., 5900, 1
Harmon, B. A., Zhang, S. N., Paciesas, W. S., & Fishman, G. J. 1993b, IAU Circ., 5874, 2
Hjellming, R. M., Rupen, M. P., Shrader, C. R., Campbell-Wilson, D., Hunstead, R. W., & McKay, D. J. 1996, ApJ, 470, L105
Ling, J. C., & Wheaton, W. A. 2003a, ApJ, 584, 399
———. 2003b, ApJ, 598, 334
———. 2005, Chinese J. Astron. Astrophys., in press (astro-ph/0409307)
Ling, J. C., Wheaton, W. A., Mahoney, W. A., Skelton, R. T., Radocinski, R. G., & Wallyn, P. 1996, A&AS, 120, 677
Ling, J. C., et al. 1997, ApJ, 484, 375
———. 2000, ApJS, 127, 79
Masetti, N., Bianchini, A., Bonibaker, J., Della Valle, M., & Viio, R. 1996, A&A, 314, 123
McConnell, M. L., et al. 2000, ApJ, 543, 928
———. 2002, ApJ, 572, 984
Meier, D. L. 2001, ApJ, 548, L9
Mirabel, F. N., Rodriguez, L. F., & Cordier, B. 1993, IAU Circ., 5876, 2
Phlips, B., et al. 1996, ApJ, 465, 907
Poutanen, J., & Coppi, P. S. 1998, Phys. Scr., T77, 57
Revnivtsev, J. P., et al. 1998, A&A, 331, 557
Shakura, N. I., & Sunyaev, R. A. 1976, MNRAS, 175, 613
Sunyaev, R. A., & Titarchuk, L. G. 1980, A&A, 86, 121
Turolla, R., Zane, S., & Titarchuk, L. 2002, ApJ, 576, 349
van der Hooft, F., et al. 1996, ApJ, 458, L75